

Emergence of intrinsic superconductivity in monolayer W_2N_3 Jianyong Chen^{1,3,*} and Yanfeng Ge²¹College of Science, Guilin University of Aerospace Technology, Guilin 541004, People's Republic of China²State Key Laboratory of Metastable Materials Science & Technology and Key Laboratory for Microstructural Material, Physics of Hebei Province, School of Science, Yanshan University, Qinhuangdao 066004, People's Republic of China³State Key Laboratory of Powder Metallurgy, and Powder Metallurgy Research Institute, Central South University, Changsha 410083, People's Republic of China (Received 28 September 2020; revised 4 January 2021; accepted 10 February 2021; published 23 February 2021)

Two-dimensional (2D) materials possessing intrinsic superconductivity with high transition temperature and unconventional pairing are highly desired, but their realizations are few and far between. Recently, W_2N_3 nanosheets down to three layers were successfully prepared [Yu *et al.*, *Adv. Mater.* **30**, 1805655 (2018)]. By performing solid *ab initio* calculations based on the anisotropic Migdal-Eliashberg theory, we predict that monolayer W_2N_3 is an unexplored intrinsic (without the assistance of external gating, strain, or a special substrate) 2D superconductor with large electron-phonon coupling (EPC) and high critical temperature $T_c = 38$ K accompanied with a single and broad superconducting gap ~ 7.5 meV. The ratio between the gap and the critical temperature is much larger than the value derived from Bardeen-Cooper-Schrieffer (BCS) theory, further confirming the strong coupling feature of monolayer W_2N_3 . The extremely strong EPC originates from the large deformation potential of low-frequency acoustic phonons rather than Fermi-surface nesting. Due to the partially filled *d* orbitals, electron-electron correlation leads to remarkable enhancement of EPC based on frozen phonon analysis. Here, T_c can be further enhanced via hydrogen passivation based on the McMillian-Allen-Dynes formula. In addition, the symmetry-restricted spin-orbit coupling (SOC) brings forth exotic type-I Ising pairing whose in-plane upper critical field is far beyond the Pauli paramagnetic limit. Our predictions provide a fascinating and highly feasible platform for realizing high-temperature 2D superconductivity and studying the interplay between electron-phonon coupling, electron-electron correlation, and SOCs.

DOI: [10.1103/PhysRevB.103.064510](https://doi.org/10.1103/PhysRevB.103.064510)**I. INTRODUCTION**

As a representative order-disorder phase transition, superconductivity is significantly affected by the dimension of materials [1]. The last two decades have witnessed the surging of two-dimensional (2D) superconductors with truly atomic-scale thicknesses and much higher crystallinity than conventional deposited thin films, driven by rapid advancements in nanotechnology, like mechanical exfoliation. The study of 2D superconductors has evolved into one of the most active fields of superconductivity, which provides a fertile land for studying exotic and intrinsic properties, like quantum phase transition, topological superconductivity, Ising superconductivity, and charge density waves (CDWs). Since the advent of graphene [2], the pursuit of 2D superconductors keeps going. The prerequisite for superconductivity is nonzero electronic density of states (DOS) at Fermi level. Therefore, charge doping or gating is a widely used strategy to induce or enhance superconductivity in 2D materials. Theoretically, graphene is predicted to be a superconductor with $T_c \sim 30$ K at extremely high doping ($4 \times 10^{14} \text{ cm}^{-2}$) and large strain (16%) levels [3]. Monolayer MoS_2 is predicted to be superconducting with a maximum T_c of 22 K at the optimal hole doping concentration of $1.6 \times 10^{14} \text{ cm}^{-2}$ and 4% biaxial compressive strain [4]. The T_c of monolayer black phosphorene is

estimated to be 17 K at the typical electron doping concentration $3 \times 10^{14} \text{ cm}^{-2}$ accompanied with 4.0% biaxial strain [5]. Another efficient strategy to induce superconductivity is depositing or intercalating alkali metal or alkali-earth metal on 2D materials. By lithium or calcium deposition, monolayer graphene is predicted to be a superconductor below 1.4 or 8.1 K, respectively [6]. It is demonstrated that the Li-intercalated bilayer MoS_2 and phosphorene are superconductors with T_c of 10 K [7] and 16.5 K [8], respectively. However, experimentally, the high-concentration doping and strain are difficult to realize, and the optimal T_c is far from reached. In the liquid-gated MoS_2 thin flake, superconductivity was reported with T_c of 7–11 K [9,10]. A superconducting transition was detected at a temperature of 7 K [11] and 4.5 K [12] in the Ca-intercalated epitaxial graphene and K-intercalated few-layer graphene. Intercalated black phosphorus is found to be superconducting with the critical temperature of only 3.8 ± 0.1 K, regardless of the kind of intercalated metals [13].

2D materials with intrinsic metallicity should be another alternative to realize superconductivity. Monolayer or few-layer 2H-NbSe₂ [14,15], 2H-TaS₂ [16], 1T_d-MoTe₂ [17], and Mo₂C [18] are confirmed to be intrinsic superconductors but with quite low transition temperature in the range of 3–7 K. Many polymorphs of borophenes, like β_{12} and χ_3 , are predicted to be intrinsic phonon-mediated superconductive with T_c of 10–20 K [19,20]. However, the synthesis of borophene is quite challenging [21], and metal substrates are detrimental to its superconductivity [22]. So far, there is no experimental

*glcyjong@guat.edu.cn

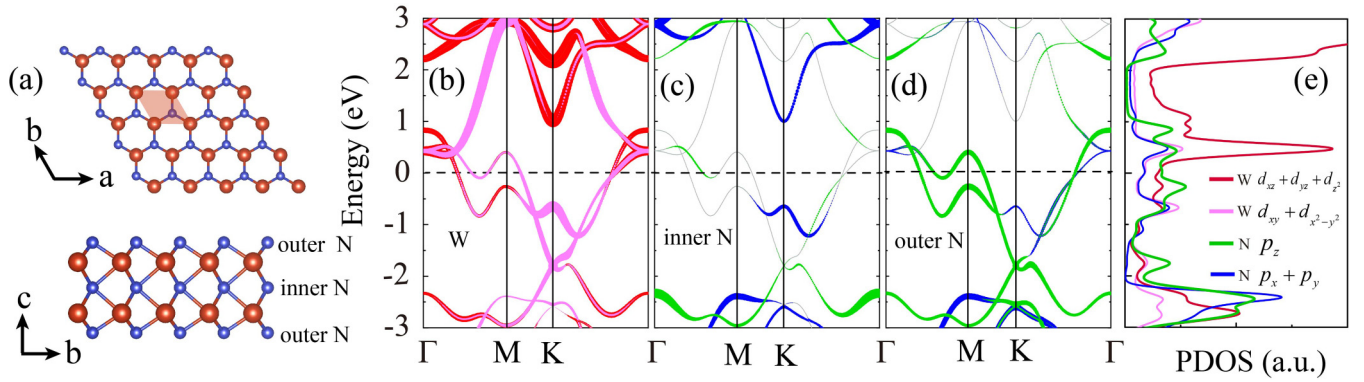


FIG. 1. (a) Top and side view of crystal structure of monolayer W_2N_3 . The filled rhombus denotes a primitive unit cell, the brown and blue balls represent tungsten and nitrogen atoms, respectively. Orbital projected band structures on (b) W atom, (c) inner layer N atom, and (d) outer layer N atom with orbital contributions proportional to the size of the colored dots. (e) Projected density of states (DOS).

report of superconductivity in borophene. Bekaert *et al.* [23] show that reducing the thickness of the bulk superconductor MgB_2 to one layer not only preserves the superconducting transition nature with $T_c = 20$ K but also leads to additional superconducting gaps. Most strikingly, the T_c of monolayer MgB_2 can be raised to 53 K [23] by applying small tensile strain and 67 K [24] by hydrogen passivation.

In this paper, we predict that monolayer W_2N_3 is an intrinsic superconductor with large electron-phonon coupling (EPC) of 1.815 and high transition temperature T_c of 38 K without the help of gating or charge doping, external strain, or chemical passivation. The T_c is nearly the same with 39 K as the famous conventional bulk superconductor MgB_2 [25] and surpasses most of the predicted and experimental reported T_c of atomic thin materials. In addition, monolayer W_2N_3 is a potential type-I Ising superconductor which can sustain extremely huge in-plane magnetic fields. The coupling mechanism, electron correlation, anisotropic, and passivation effect are discussed in detail as well. Considering the successful preparation of few-layer (~ 1.5 nm) 2D hexagonal W_2N_3 flakes at atmospheric pressure via a salt-templated method [26], the predicted exotic superconductivity will be attainable by experiment in the near future.

II. METHODS

First-principles calculations were performed within the density functional theory (DFT) as implemented in the well-established Quantum-ESPRESSO package [27]. The Perdew-Burke-Ernzerhof parameterized generalized-gradient approximation (PBE-GGA) [28] was used to describe the exchange correlation. Projector-augmented wave (PAW) potentials were adopted to represent the interaction between ionic cores and valence electrons. A sufficiently thick vacuum (15 Å) was added in the model to avoid nonphysical coupling between adjacent images. A plane-wave basis with a 60 Ry energy cutoff was used to represent electronic wave functions. All structures were fully relaxed until the forces were smaller than 1×10^{-5} Ry/a.u. The dynamical matrices and the EPC were calculated using density functional perturbation theory (DFPT) [29] in the linear response regime, which were used as the input for solving the anisotropic

Eliashberg equations. The dynamical matrix was computed on $8 \times 8 \times 1$ Monkhorst-Pack (MP) [30] \mathbf{q} -point grids. The EPC converges when adopting a fine $32 \times 32 \times 1$ \mathbf{k} -point grid with a Marzari-Vanderbilt [31] smearing of 0.02 Ry. Carrier doping was simulated with a jellium model, where excess or defect electronic charge was compensated by a uniform neutralizing background. Computational details of EPC constant, anisotropic Migdal-Eliashberg equations, spin texture plots, converge tests of phonon dispersion, and superconducting gaps are given in Appendices A–D.

III. RESULTS AND DISCUSSIONS

Each unitcell of bulk W_2N_3 consists of two layers of W_2N_3 with W(N) atoms in one layer located precisely on top of N(W) atoms in the other layer. The inversion symmetry is preserved in bulk W_2N_3 (space group $P6_3/mmc$). Figure 1(a) shows the top and side view of the crystal structure of monolayer W_2N_3 . The W and N layers stack alternately. Each W atom is bonded with six N atoms. N atoms are divided into two categories. Each inner layer N is bonded with six W atoms, and the outer layer N is bonded with three W atoms. The monolayer W_2N_3 possesses out-of-plane mirror symmetry but broken inversion symmetry. It belongs to the $P\bar{6}m2$ space group. The optimized in-plane lattice constant and thickness of monolayer W_2N_3 are 2.91 and 5.15 Å, respectively. The lattice constant agrees well with experimental results of 2.90 Å [26], but the calculated thickness deviates 6% from experimentally determined 5.5 Å for few-layer W_2N_3 [32]. We have rechecked the thickness by considering spin-orbit coupling (SOC), onsite Coulomb repulsion, different pseudopotentials, and different PBE functionals. All calculated thicknesses fall in the range of 5.17–5.22 Å, which are consistent with other calculations ~ 5.17 Å [33,34]. The discrepancy between theory and experiments may be accounted for by the high temperature (1480 K) fabrication condition [35]. In fact, our ongoing research reveals that another bulk compound composed of W_2N_3 layers (not the layered bulk counterpart of monolayer W_2N_3) also shows quite strong EPC and high T_c . The EPC in monolayer W_2N_3 may be not sensitive to the thickness but inherited in the strong W-N bonding. Figures 1(b)–1(d) display the orbital projected band

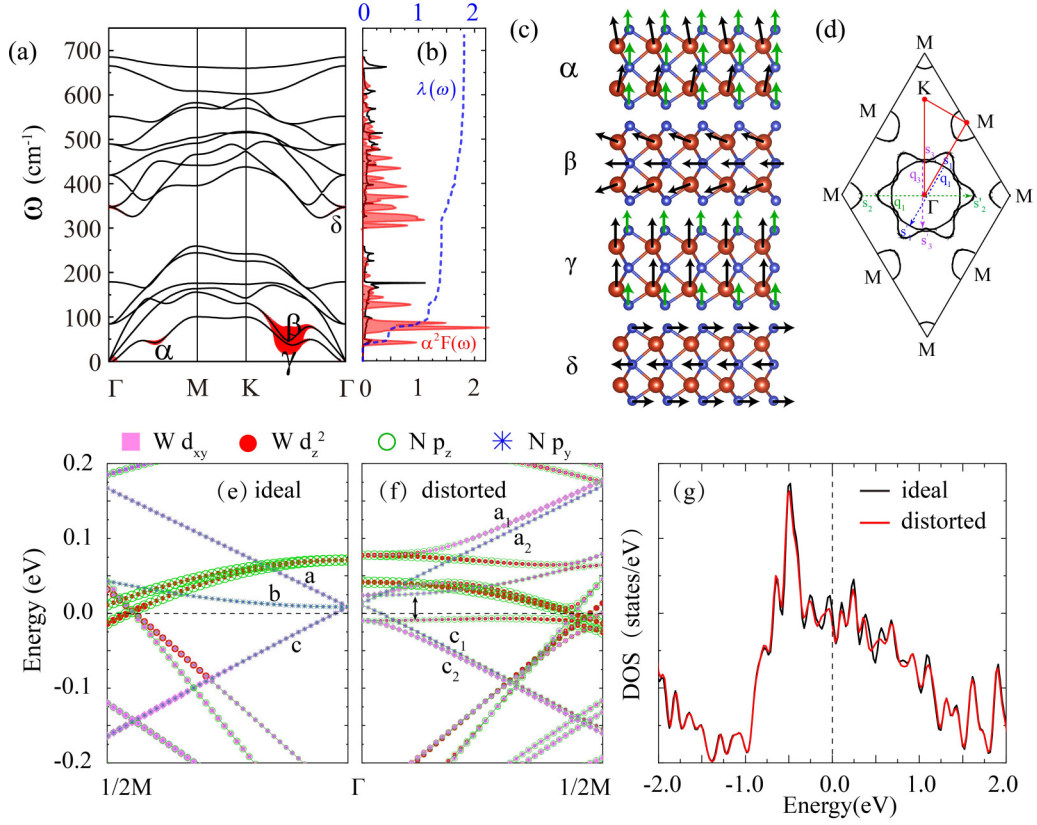


FIG. 2. (a) Phonon dispersion decorated with red dots proportional to the partial electron-phonon coupling strength $\lambda_{\mathbf{q}\nu}$. (b) Phonon density of states (PHDOS) (black solid line), isotropic Eliashberg spectral functions $\alpha^2F(\omega)$ (pink shaded region) and cumulative frequency-dependent coupling $\lambda(\omega)$ (blue dashed line). (c) Schematic illustration of the vibrational pattern in real space with large $\lambda_{\mathbf{q}\nu}$ for α , β , γ , and δ modes. The length of the arrows is proportional to the amplitude of vibration. (d) Fermi surface and the major nesting wave vectors (color arrows) connecting the strong nesting pieces of Fermi surface. Calculated band structures of monolayer W_2N_3 in a $6 \times 6 \times 1$ supercell (e) before and (f) after being distorted by the ZA phonon at $1/2M$ of the primitive cell. The band is plotted from the Γ point to $1/2M$ of the $6 \times 6 \times 1$ supercell Brillouin zone. (g) Total DOS of the $6 \times 6 \times 1$ supercell.

structures of monolayer W_2N_3 on $W d$ and $N p$ orbitals. Three bands intersect the Fermi level, and they all form hole pockets. The three bands show strong mixing of in-plane and out-of-plane states. For instance, the band spanning from -1.0 to 0.9 eV is composed of both out-of-plane orbitals from $W d_{xz} + d_{yz} + d_z^2$ and $N p_z$ along the Γ - M direction and in-plane orbitals from $W d_{xy} + d_{x^2+y^2}$ and $N p_x + p_y$ along the Γ - K direction. The inner-layer N atoms contribute little to the states at Fermi level, as shown in Fig. 1(c). By comparing the relative height of DOS in Fig. 1(e), one can infer that both the out-of-plane and in-plane states contribute to DOS at Fermi level, where the proportion of out-of-plane states are slightly larger. This indicates that vibration modes along the z direction (γ mode) will couple strongly with these electrons.

Next, we discuss the central quantity in superconductivity, namely the EPC constant λ and superconducting critical temperature T_c . The former can be calculated through the isotropical momentum-independent Eliashberg function [36] (see Appendix A for details). Here, T_c is estimated by the McMillian-Allen-Dynes formula [37,38]:

$$T_c = f_1 f_2 \frac{\omega_{\log}}{1.2} \exp \left[\frac{-1.04(1 + \lambda)}{\lambda - \mu^*(1 + 0.62\lambda)} \right], \quad (1)$$

where ω_{\log} is the logarithmic average of the phonon frequencies. The retarded Coulomb pseudopotential μ^* in Eq. (1) measures the strength of electron-electron interaction [39]. It is determined to be 0.17 for monolayer W_2N_3 based on $\mu^* \approx \{0.26N(E_F)/[1 + N(E_F)]\}$, which is deemed suitable to describe electron-electron interactions in d -band metals and has been widely used [40,41]. Here, f_1 and f_2 are strong coupling and shape corrections:

$$f_1 = \left\{ 1 + \left[\frac{\lambda}{2.46(1 + 3.8\mu^*)} \right]^{3/2} \right\}^{1/3}, \quad (2)$$

$$f_2 = 1 + \frac{[(\omega_2/\omega_{\log}) - 1]\lambda^2}{\lambda^2 + 3.312(1 + 6.3\mu^*)^2(\omega_2/\omega_{\log})^2}, \quad (3)$$

in which ω_2 is defined as

$$\omega_2 = \left[\frac{2}{\lambda} \int_0^{\omega_{\max}} \alpha^2 F(\omega) \omega d\omega \right]^{1/2}.$$

Figure 2(a) presents the phonon dispersion decorated with red dots that is proportional to the partial EPC strength $\lambda_{\mathbf{q}\nu}$ (see the definition in Appendix A). The absence of imaginary phonons confirms the dynamical stability of monolayer W_2N_3 . By calculating the cumulative frequency-dependent

$\lambda(\omega)$ in Fig. 2(b), one can figure out that the EPC are dominated by acoustic phonons. Those phonons below 100 cm^{-1} contribute 64% ($1.170/1.815 = 64\%$) of the total EPC. The middle range optical modes spanning from 100 to 350 cm^{-1} also make significant contributions to EPC. The four conspicuously large λ_{qv} are labeled with α , β , γ , and δ in Fig. 2(a), and corresponding vibration patterns are depicted in Fig. 2(c). Two out of three acoustic branches correspond to vibration within the plane [longitudinal acoustic (LA) and transverse acoustic (TA)], and the other corresponds to vibration out of the plane (ZA). For 2D materials with reflection symmetry, ZA modes are forbidden to participate in intraband EPCs within the first-order approximation [42,43], which is true in single Fermi sheet materials, like hole-doped graphene [44], hole doped h-BN [45], and electron-hole-doped monolayer MoS_2 [4]. However, there are multiple pieces of Fermi sheet in monolayer W_2N_3 , as show in Fig. 2(d). The ZA phonon can participate in interband coupling (this accounts for the large λ_{qv} for the α and γ modes). The β mode involves the in-plane vibration of W and inner-plane N atoms. The upper- and lower-layer W atoms have tiny out-of-plane vibrations against each other. The γ mode is associated with the out-of-plane vibration of W atoms and outer side N atoms; W atoms have a relatively large vibration amplitude. In this mode, the inner N atoms remain silent. The δ mode originates from the in-plane oscillation of N atoms; the two outer side N atoms move as a whole and go the opposite direction from the inner-layer N atoms. Based on the above analysis, we can infer that both in-plane and out-of-plane vibrations contribute to EPC, consistent with the reasoning from electronic states. Based on the McMillian-Allen-Dynes formula (Appendix E), T_c is estimated to be 24.58–20.06 K with μ^* from 0.10 to 0.17. Figure 2(d) gives the major nesting wave vectors connecting the strong nesting pieces of the Fermi surface. The \mathbf{q}_1 (\mathbf{q}_2) nesting vector connect the two parallel linelike (circlelike) Fermi pockets S_1 (S_2) and S'_1 (S'_2) along the Γ - M direction. This Fermi nesting explains partly the large λ_{qv} at the α point. The \mathbf{q}_3 nesting vector connects the double linelike S_3 and S'_3 along the Γ - K direction, which is responsible for the pronounced phonon softening of β and γ along Γ - K . As shown in Fig. 2(b), the height and energy position of $\alpha^2 F(\omega)$ peaks strikingly differ from phonon DOS (PHDOS), which is like the strong anisotropic superconductor MgB_2 [46]. The anisotropic coupling effect will be discussed in the latter part of this paper.

It is important to clarify why α , β , γ , and δ modes have large EPC. Anomalous large EPC strength of specific phonons stems either from strong Fermi-surface nesting [47] or deformation potential (breaking of electronic degeneracies by lattice vibration) [48]. The former mechanism can be ruled out in monolayer W_2N_3 because there are no large pieces of parallel Fermi surfaces showing strong nesting, as shown in Fig. 2(d). Most importantly, the nesting vectors do not match the phononic wave vector where the most softened phonon occurs. To test the latter mechanism, we investigated the γ mode perturbed electronic properties at the $1/2M$ point as an example. A $6 \times 6 \times 1$ supercell was constructed to fold $1/2M$ of a primitive cell into the Brillouin zone center of the supercell. Figures 2(e)–2(g) show the calculated band structures and DOS before and after being distorted by the

γ mode. The Fermi level of the ideal monolayer locates at the shoulder of the DOS peak, which is an indicator of strong EPC. The $N(E_F)$ decreases when the structure is distorted by the given phonon. Meanwhile, the band degeneracy at the Γ point of the supercell is removed. The degenerate band near the Fermi level at the Γ point, denoted as a , splits into a_1 and a_2 bands with a splitting energy of 62.8 meV. The degeneracy of band b is also removed, which splits into two bands below and above the Fermi level, denoted by the black arrow, with a splitting energy 33.5 meV at Γ . The splitting of band c bears a resemblance to the case of the a and b bands but with a much lower splitting energy. The phonon-induced breaking of electronic degeneracies plays a dominant role in the phonon softening and anomalous large EPC strength [48,49].

The correlation effect is expected to be strong in monolayer W_2N_3 because there are partially filled d electrons near the Fermi level. The GGA or local-density approximation usually underestimates EPC due to the overestimation of dielectric screening and underestimation of the bandwidth [50]. However, it is not a universal law and is quite system dependent. For example, electron correlation strongly enhanced EPC in 2D graphene [51], Li_xZrNCI [52], and high- T_c superconductors, like $\text{Ba}_{n+1}\text{Bi}_n\text{O}_{3n+1}$ and ZrNCI [50]. On the contrary, EPC calculated with electron correlation is reduced by a factor of 2 and 25 for MoS_2 thin flakes and FeB_4 , respectively [53,54].

To evaluate the effect of electron-electron correlation on the EPC of a specific phonon, a frozen phonon band calculation with both the GGA and the HSE06 functional ($\mu = 0.2$, $\alpha = 0.25$) is adopted [50]. The splitting energy of bands perturbed by the E' phonon at the Γ point is 0.312 eV with HSE06 ($\mu = 0.2$, $\alpha = 0.25$) and 0.294 eV with self-consistent quasiparticle GW calculation (GW0 calculation converged with 300 empty bands). Therefore, the nonlocal exchange correlation can be well described by HSE06. The EPC strength can also be expressed as

$$\lambda = \frac{2}{N(E_F)N_q} \sum_{k,q,v} |M_{k,k+q}^v|^2 \frac{\delta(\varepsilon_k - \varepsilon_F)\delta(\varepsilon_{k+q} - \varepsilon_F)}{\omega_{qv}}, \quad (4)$$

where N_q is the number of q points, $M_{k,k+q}^v$ is the reduced electron-phonon matrix element (REPME); note that the square of REPME contributes to λ . The REPME can be derived from the splitting energy of bands in the frozen phonon calculations. First, the bandwidth of the band intersecting the Fermi level spanning from -1.2 to 0.8 eV is 2 eV within the GGA level [Fig. 3(a)], while the bandwidth increases remarkably to 2.8 eV at the HSE06 level [Fig. 3(b)]. This underestimation of bandwidth indicates an underestimation of REPME by GGA. For the E' phonon at the Γ point (δ point), the primitive cell is used for the frozen phonon calculation. As can be seen in Fig. 3(a) and 3(b), the band splittings indicated by the arrows close to the Fermi energy are 0.262 eV for the GGA and 0.312 eV for the HSE06 calculations perturbed by E' phonon modes at the Γ point upon a displacement of 0.04 Å. The corresponding REPME are $|M_{\text{GGA}}| = 3.28 \text{ eV/\AA}$ and $|M_{\text{HSE06}}| = 3.90 \text{ eV/\AA}$, which means that the EPC of the E' mode is enhanced by a factor of 1.42 ($|M_{\text{HSE06}}|^2/|M_{\text{GGA}}|^2$). The α mode locates at $1/2M$. A unit cell of the displaced structures is constructed by a $4 \times 1 \times 1$ supercell to commensurate

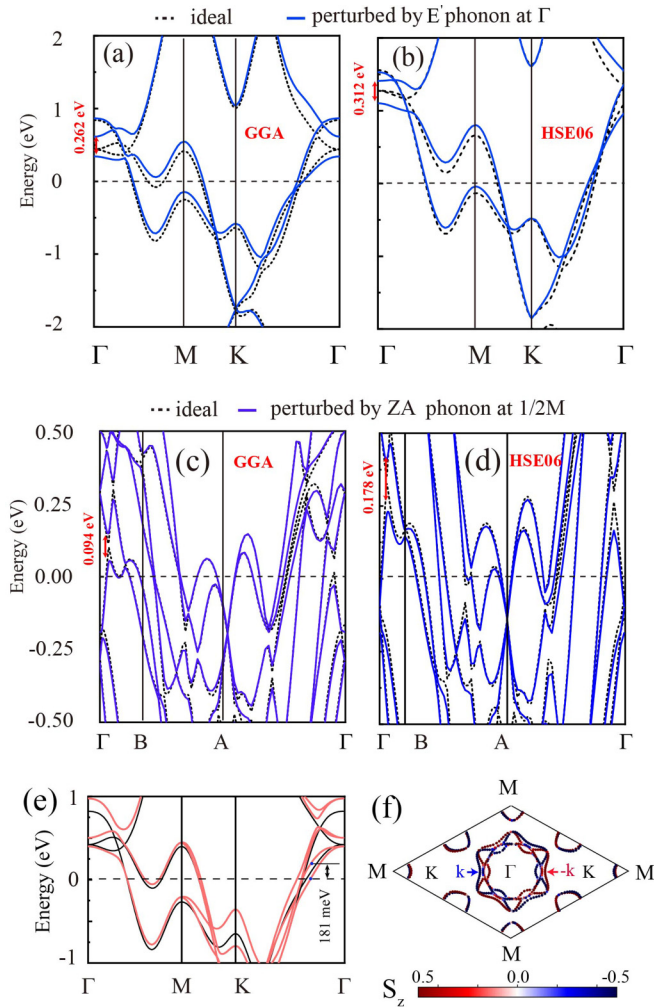


FIG. 3. The blue lines represent the band structures perturbed by (a) and (b) the E' phonon at the Γ point and (c) and (d) the ZA phonon at $1/2K$ with the frozen phonon calculations. (a) and (b) are calculated with the primitive cell, and (c) and (d) are calculated with a $4 \times 1 \times 1$ supercell. The black dashed lines denote the bands of undistorted structures. The maximum displacement of the atom is 0.04 Å in the calculations. (e) Electronic structure with (red) and without (black) SOC included. Spin texture at the Fermi level in monolayer W_2N_3 . The color in (f) represents the out-of-plane spin polarization $\langle S_z \rangle$.

with the \mathbf{q} vector of the phonon. The band splittings near the Γ point are about 0.094 eV [Fig. 3(c)] for the GGA and 0.178 eV [Fig. 3(d)] for the HSE06 calculations, resulting in a REPME of 1.18 and 2.23 eV/Å, respectively. The HSE06 treatment enhances the EPC of the ZA mode remarkably by a factor of 3.57, even stronger than that brought by the oxygen-breathing mode at the R point in the strongly correlated superconductor $BaBiO_3$ [50]. As the evaluation of the total EPC strength requires the summation of all phonons in the entire Brillouin zone which is out of our reach at present, we cannot estimate the correlation-enhanced T_c (one can refer to the paper by Li *et al.* [55]). We just go one step further than DFT GGA and emphasize that the nonlocal electron-electron correlation is important in describing the EPC of monolayer W_2N_3 .

For conventional superconductors with atomic thickness, coupling between the electron momentum and the magnetic field are significantly eliminated by quantum confinement. The in-plane upper critical field at zero temperature is dictated merely by Zeeman splitting energy, known as the Pauli paramagnetic limit $H_p = (1.86 \text{ TK}^{-1})T_c(0)$ [56,57]. Surprisingly, experimentally observed in-plane upper critical field in gated 2H-MoS₂ [10], 2H-NbSe₂ [14,15], and 2H-TaS₂ [16] exceeds the Pauli limit by threefold to fivefold, which is called Ising superconductivity. Next, we show that, apart from strong correlation effect, the W 5 d electrons also give rise to strong relativistic effects. SOC splits the originally degenerate conduction bands where the spin splitting energy is 181 meV along the Γ - M direction [Fig. 3(e)]. Figure 3(f) and Appendix F present the spins projected along $\langle S_z \rangle$, $\langle S_x \rangle$, and $\langle S_y \rangle$ and the direction at the Fermi level. There is only tiny $\langle S_x \rangle$ components along the Γ - M direction, and the $\langle S_y \rangle$ component is vanishing. Therefore, electrons at Fermi energy are fully spin polarized in the out-of-plane direction. Most importantly, electrons with opposite momenta are antiparallel to each other. This Zeeman-like SOC is consistent with the underlying mechanism of Ising superconductivity, which locks the spins of Cooper pairs in the out-of-plane direction and is immune to limited in-plane magnetic field [10]. According to the Pauli paramagnetic limit, H_p is determined to be 70 T for monolayer W_2N_3 with T_c of 38 K. As a potential Ising superconductor, the actual in-plane upper critical field that the monolayer can sustain may be >70 T.

It is necessary to investigate the effect of strain and charge doping on superconductivity, as it is experimentally found that the abundance of N vacancies in 2D W_2N_3 increases when the thickness decreases [32], resulting in a natural chemical and charge doping. Additionally, 2D materials are inevitably grown on substrate, which will exert strain on the 2D films. The total EPC strength and distribution of EPC in the phononic wave vector space, especially the ones at β and γ , are significantly affected by doping and strain (see Appendix G for details). However, the $N(E_F)$, the size of the Fermi surface, and topology remain intact upon doping or strain (see Appendices E and G for details). We therefore reiterate that Fermi surface nesting is not responsible for the strong EPC in monolayer W_2N_3 . Meanwhile, superconductivity is suppressed by hole doping and tensile strain (see Appendix E). To maximally preserve the superconducting states, a substrate that can donate electrons to and compress the 2D W_2N_3 films is preferred.

Considering the reduced dimensionality in monolayer materials and anisotropic EPC, the isotropic approximation embedded in the Allen-Dynes formula may fail in accurately describe the EPC and the superconducting gap. To examine the anisotropy effect, we solve the fully anisotropic Migdal-Eliashberg equations self-consistently using the EPW code [58,59]. The maximally localized Wannier function (MLWF) interpolated band structure fitted well with DFT calculations, as shown in Fig. 4(a), which lays a solid foundation for subsequent EPW calculation. The Hamiltonians and the dynamical matrix in Wannier representation $[H(R)]$ show exponential decay with increasing R (Appendix C), indicating that the electron Hamiltonian and phonon dynamical matrix in the Wannier basis are sufficient to interpolate EPC. To quantify

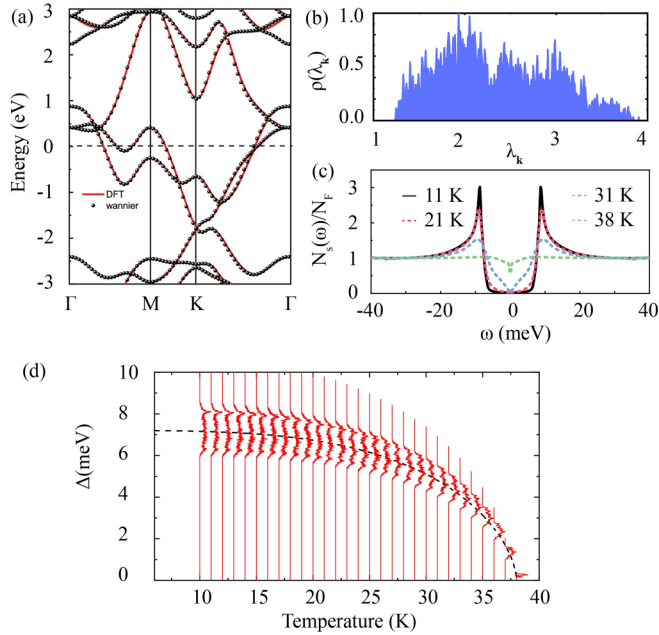


FIG. 4. Anisotropic effect in monolayer W_2N_3 . (a) Comparison of band structure obtained by density functional theory (DFT) (red lines) and interpolation with maximally localized Wannier functions (MLWFs) (black dots). (b) Distribution of the anisotropic electron-phonon coupling (EPC) strength $\lambda_{\mathbf{k}}$. (c) Corresponding quasiparticle density of states (DOS) for four representative temperatures. Quasiparticle DOS in the superconducting state, relative to the DOS in the normal state $N_s(\omega)/N_N(\omega)$, as a function of frequency. The superconducting DOS is scaled to coincide with normal DOS, which can facilitate comparing with experimental detection. (d) Energy distribution of the anisotropic superconducting gap as a function of temperature.

the anisotropy of EPC, band- and wave-vector-dependent EPC strength defined by $\lambda_{\mathbf{k}} = \sum_{\mathbf{k}'} W_{\mathbf{k}\mathbf{k}'} \lambda(\mathbf{k}, \mathbf{k}', n=0)$ are shown in Fig. 4(b). The wide spread of $\lambda_{\mathbf{k}}$ between 1.23 and 3.83 reveals a strong anisotropic coupling. The quasiparticle DOS at 11, 21, 31, and 38 K for monolayer W_2N_3 are plotted with respect to the normal DOS in Fig. 4(c). The position of the superconducting quasiparticle DOS peak coincides with the superconducting gap in Fig. 4(d) at the same temperatures. The one-gap nature is reflected directly by the single sharp peak in superconducting DOS in Fig. 4(c). Figure 4(d) shows the temperature evolution of the superconducting energy gap $\Delta_{\mathbf{k}}$ by solving the Eliashberg equations for each temperature with $\mu^* = 0.1$, which obviously display a single gap with an anisotropic and broad energy spreading from 6.3 to 8.9 meV at 10 K. The gap and the quasiparticle DOS vanish at 38 K, which is identified as the critical temperature T_c . This T_c enhances the isotropical value of 24.58 K by 55%, confirming that the anisotropic effect is important in describing the superconducting properties. The anisotropic Migdal-Eliashberg theory considers the variation of electron-phonon interaction on the full Fermi surface, but the McMillian-Allen-Dynes formula assumes isotropical coupling. Underestimation of T_c by the latter method is ubiquitous in anisotropical superconductors, like monolayer graphene [44], borophene [60], and MgB_2 [61]. To shed light on the formation of a single gap,

we compare the bands of monolayer W_2N_3 with the multi-gap superconductors. The bands crossing the Fermi level in multi-gap superconductors, like borophene [60], MgB_2 [46], and AlB_2 [62], are highly direction resolved. Taking MgB_2 as an example, two cylindrical sheets arise from quasi-2D $\sigma(s + p_{x,y})$ states, and two tubular networks originate from $\pi(p_z)$ states [63]. The difference in character between the Fermi sheets leads to the two-gap nature. Meanwhile, the interband coupling between the σ - and π -bonding Fermi surface is small, which avoids the overlap of the two gaps. In contrast, the bands crossing the Fermi level in W_2N_3 [Figs. 1(b)–1(d)] show strong mixing of in-plane and out-of-plane states, and the phonon-assisted interband coupling is strong [Fig. 2(d)]. These two factors account for the one-gap nature and its wide spread. The ratio between the gap and the critical temperature is $2\Delta_0/k_B T_c = 4.30$, larger than the value of 3.52 for a weak-coupling superconductor derived within the Bardeen-Cooper-Schrieffer (BCS) theory, again confirming that monolayer W_2N_3 is a strong-coupling superconductor.

To further promote the superconducting critical temperature, we consider the hydrogen passivation strategy, which is proved to be quite successful in enhancing the T_c in 2D materials, like monolayer MgB_2 [24]. The passivated monolayer $W_2N_3-H_2$ is proved to satisfy the energetic, thermal, dynamical, and mechanical stability criteria (see Appendix H for detail). As shown in Fig. 5(a), passivation significantly modifies the band profile, and Fermi surface pockets are transferred from hole pockets (in pristine W_2N_3) to electron pockets. The total DOS at Fermi level decreases slightly (see Appendix E). As shown in Fig. 5(b), the out-of-plane states of W d orbitals surpass the in-plane states at the Fermi energy, which remain in the same order in pristine monolayer W_2N_3 . In contrast, the contribution of N $p_x + p_y$ states is larger than N p_z orbitals, which is inversely true in pristine monolayer. Here, H s orbitals also contribute to $N(E_F)$. The peak positions of H s states coincide with that of N p_z states, highlighting a hybridization with the N p_z states. The change of electronic states will bring profound influence on the EPC. Figure 5(c) gives the phonon dispersion decorated with red dots proportional to the partial EPC strength $\lambda_{q\nu}$. The phonon dispersion changes remarkably by passivation. The soft phonons of β and γ are hardened, and their $\lambda_{q\nu}$ decrease. There is an obvious frequency gap of $\sim 2463 \text{ cm}^{-1}$ due to the large mass difference between nitrogen and hydrogen. The largest $\lambda_{q\nu}$ labeled by α is no longer at $1/2K$ but moves to the M point due to the change of Fermi surface topology. In addition, the vibration of mode α is associated with both in-plane and out-of-plane displacement, which is different from the pure out-of-plane oscillation (γ mode) in W_2N_3 . This is understandable because N $p_x + p_y$ orbitals make great contribution to $N(E_F)$. Note that the vibration amplitude of H atoms is large in α and β mode, indicating its nonnegligible contribution to EPC. The phonons below 600 cm^{-1} originating from W and N atoms contribute 88% of the total λ [Fig. 5(d)], indicating that the superconductivity is inherited in pristine W_2N_3 . Hydrogen passivation weakens the total EPC strength from 1.815 to 1.066, but the hydrogen-related high-frequency phonons lead to a significant boost of ω_{log} from 155.785 K in pristine monolayer to 349.674 K. Based on the McMillian-Allen-Dynes formula (Appendix E), T_c is finally raised to 29.21–22.27

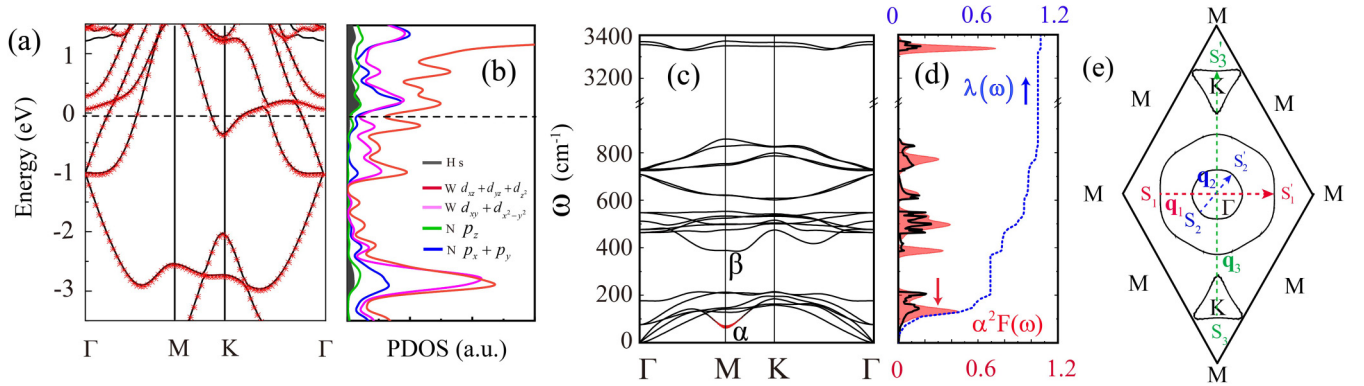


FIG. 5. (a) Band structures of monolayer $W_2N_3-H_2$ by density functional theory (DFT) (black lines) and interpolation with maximally localized Wannier functions (MLWFs) (red asterisk). (b) Projected density of states (DOS). (c) Phonon dispersion decorated with red dots proportional to the partial electron-phonon coupling strength λ_{qv} . (d) Phonon DOS (PHDOS) (black solid line), $\alpha^2F(\omega)$ (pink shaded region) and $\lambda(\omega)$ (blue dashed line). (e) Fermi surface and the major nesting wave vectors (color arrows) connecting the strong nesting pieces of Fermi surface.

K with μ^* from 0.10 to 0.17. The Fermi surface topology changes upon hydrogen passivation [Fig. 5(e)]. The ellipse-like Fermi pocket around the M point in pristine W_2N_3 is removed. There emerges a triangle pocket centered around the K and $-K$ points. Meanwhile, the flowerlike pocket around Γ is replaced by a large regular hexagon with round corners. There is a strong nesting between the large parallel linelike S_1 , S'_1 , and S_2 , S'_2 along the Γ - M direction by the nesting vector \mathbf{q}_1 and \mathbf{q}_2 . Along the Γ - K direction, \mathbf{q}_3 connects S_3 and S'_3 . Similarly, the other two sides of the triangle can also be connected by a \mathbf{q} vector. The nesting of monolayer $W_2N_3-H_2$ is much stronger than that in the pristine W_2N_3 . Because the Fermi surface and nesting vectors are highly isotropic, we can see that the peaks of $\alpha^2F(\omega)$ coincide with that of PHDOS [Fig. 5(d)], demonstrating an isotropic EPC and potential s -wave superconductivity. The strong anisotropy in pristine W_2N_3 and isotropy in the hydrogen-passivated monolayer W_2N_3 illuminate us that not only crystal structure symmetry in real space but also the electronic properties in reciprocal space determine the anisotropy of the EPC.

Before concluding, we discuss the reliability of the most important finding of this paper, i.e., the T_c value. It is guaranteed by the good fitting of the electronic bands, rapid decay of the electronic Hamiltonian, dynamical matrix and electron-phonon matrix elements in the Wannier representation. In addition, the anisotropic EPC and the superconducting gap with various \mathbf{k} and \mathbf{q} meshes are tested and well converged. The superconducting gap (6.3–8.9 meV) and critical temperature (38 K) of monolayer W_2N_3 resembles the ~ 7.2 meV of the σ gap and $T_c \sim 39$ K in MgB_2 with the same calculation methods [64,65], reflecting the rationality of our EPW calculations. We have also calculated the EPC of several \mathbf{q} points with SOC included. Results show that the SOC leads to an increasing of the partial EPC strength λ_{qv} by $\sim 9\%$ (this is part of our future work). Going beyond GGA, electron-electron correlation further enhances the EPC, as demonstrated by the concrete analysis of E' and ZA modes above. Therefore, the realistic T_c of monolayer W_2N_3 may be even higher than the value of 38 K predicted in this paper.

Due to the extremely large EPC of the acoustic modes, one may suspect the stability of the structure. As a preliminary

judgment, we calculated the phonon dispersion of freestanding monolayer W_2N_3 by decreasing the smearing to 0.008 Ry. There appears an obvious imaginary phonon of -59 cm^{-1} between Γ and M , as shown in Appendix I. However, decreasing the smearing width only cools down the electrons in the system. Thermal (and quantum) fluctuations of ions are not considered. Additionally, our calculations are based on harmonic approximation. That is to say, the imaginary phonon here does not ensure a CDW instability. For instance, the calculated harmonic phonon dispersion of bulk $2H-NbS_2$ exhibits a remarkable negative phonon at the M point, but no CDW signature is observed in experiments down to the temperature of 2 K. Bianco *et al.* [66] revealed that only by considering the quantum anharmonic effects at nonperturbative level can provide quantitative agreement of phonons with experiment. Furthermore, our calculations demonstrate that small compressive biaxial strain ($\varepsilon = -0.5\%$) can effectively suppress the potential CDW transformation evidenced by their positive phonons, as shown in Appendix I. Meanwhile, the EPC strength and superconducting transition temperature remains nearly unchanged, as listed in Table I.

IV. CONCLUSIONS

In summary, by solving the anisotropic Eliashberg equations accurately with full *ab initio* input, we predict that 2D monolayer W_2N_3 is an unexplored superconductor with high transition temperature T_c of 38 K. The extraordinarily strong EPC is accounted for by the large deformation potential of low-frequency acoustic phonons. Due to the strong mixing of in-plane and out-of-plane states, monolayer W_2N_3 exhibits a single and broad superconducting gap with an average of ~ 7.5 meV. The ratio between the gap and the critical temperature is much larger than the value for a weak-coupling BCS superconductor, further confirming that monolayer W_2N_3 is a strong-coupling superconductor. The heavy element W and half-filled d orbitals give rise to enhancement of EPC for some vibration modes by electron correlation and simultaneously bring forth exotic Ising pairing, which can sustain extremely huge in-plane magnetic fields. Through hydrogen passivation, the transition temperature T_c can be greatly en-

hanced. By investigating the effect of strain and doping on superconductivity, we suggest that a substrate that can donate electrons to and compress the 2D W_2N_3 films is preferred. As few-layer W_2N_3 flakes at atmospheric pressure are successfully prepared, the predicted exotic superconductivity will be attainable by experiment in the near future.

ACKNOWLEDGMENTS

This paper was supported by the National Natural Science Foundation of China (Grant No. 51272291), Guangxi Natural Science Foundation (Grant No. 2019GXNSFBA245077), and the Scientific Research Fund of Guilin University of Aerospace Technology. J.C. was supported by Gunagxi Project of Thousand Backbone Teachers. The authors thank Fangping Ouyang for providing part of the computational resources.

APPENDIX A: COMPUTATIONAL DETAILS

The maximally localized Wannier functions (MLWFs) [67] are constructed on a uniform unshifted $12 \times 12 \times 1$ \mathbf{k} -point grid; N sp^3 and W d orbitals are chosen as projectors. The interpolated \mathbf{k} - and \mathbf{q} -point grids of $156 \times 156 \times 1$ and $78 \times 78 \times 1$, respectively, are used to solve the anisotropic Migdal-Eliashberg equations. The Matsubara frequency cutoff is set to five times the largest phonon frequency, and the Dirac δ functions are replaced by Lorentzians of widths 25 and 0.05 meV for electrons and phonons, respectively. Electrons within ± 200 meV from the Fermi energy are taken into the electron-phonon coupling (EPC) process.

The EPC constant λ and logarithmic average of the phonon frequencies ω_{\log} can be calculated through the isotropical momentum-independent Eliashberg function [36]:

$$\alpha^2 F(\omega) = \frac{1}{2\pi N(E_F)} \sum_{\mathbf{q}\nu} \frac{\gamma_{\mathbf{q}\nu}}{\omega_{\mathbf{q}\nu}} \delta(\omega - \omega_{\mathbf{q}\nu}), \quad (\text{A1})$$

$$\omega_{\log} = \exp \left[\frac{2}{\lambda} \int_0^{\omega_{\max}} \alpha^2 F(\omega) \frac{\ln(\omega)}{\omega} d\omega \right], \quad (\text{A2})$$

$$\lambda = 2 \int_0^{\infty} \frac{d\omega \alpha^2 F(\omega)}{\omega} = \sum_{\mathbf{q}\nu} \lambda_{\mathbf{q}\nu}, \quad (\text{A3})$$

where $\alpha^2 F(\omega)$ is the Eliashberg function and $N(E_F)$ is the density of states (DOS) per atom and spin at the Fermi energy, $\omega_{\mathbf{q}\nu}$ is the phonon frequency of the phonon mode ν with wave vector \mathbf{q} , and cumulative EPC is then given by

$$\lambda(\omega) = 2 \int_0^{\omega} \frac{d\omega' \alpha^2 F(\omega')}{\omega'}. \quad (\text{A4})$$

The EPC constant $\lambda_{\mathbf{q}\nu}$ for mode ν at wavevector \mathbf{q} is defined as $\lambda_{\mathbf{q}\nu} = \gamma_{\mathbf{q}\nu} / [\pi \hbar N(E_F) \omega_{\mathbf{q}\nu}^2]$. The phonon linewidth stems from the Fermi ‘‘golden rule,’’

$$\gamma_{\mathbf{q}\nu} = 2\pi \omega_{\mathbf{q}\nu} \sum_{\mathbf{k}j} \left| g_{\mathbf{k}+\mathbf{q}j', \mathbf{k}j}^{\mathbf{q}\nu} \right|^2 \delta(\varepsilon_{\mathbf{k}j} - \varepsilon_F) \delta(\varepsilon_{\mathbf{k}+\mathbf{q}j'} - \varepsilon_F), \quad (\text{A5})$$

where the Dirac δ functions express energy-conservation requirements, $\varepsilon_{\mathbf{k}j}$ is the one-electron band energy with momentum \mathbf{k} and band index j , and the screened electron-phonon

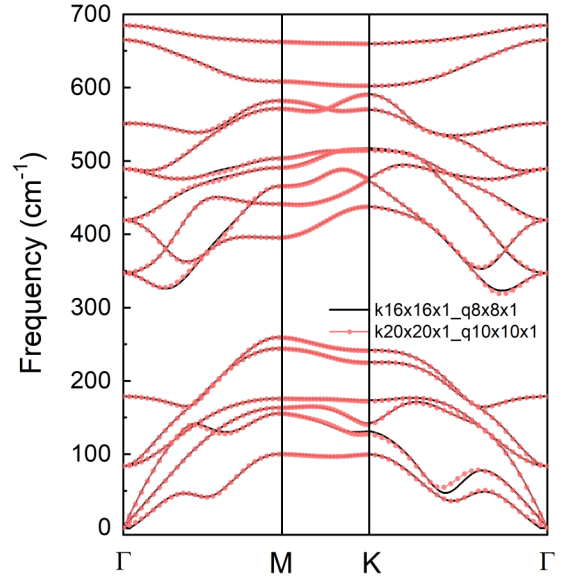


FIG. 6. Phonon dispersion of monolayer W_2N_3 with $16 \times 16 \times 1$ \mathbf{k} mesh and $8 \times 8 \times 1$ \mathbf{q} mesh and $20 \times 20 \times 1$ \mathbf{k} mesh and $10 \times 10 \times 1$ \mathbf{q} mesh.

matrix element is defined as

$$g_{\mathbf{k}+\mathbf{q}j', \mathbf{k}j}^{\mathbf{q}\nu, jj} = \sum_{R, \nu} \frac{\eta_{\mathbf{q}\nu}(R, \nu)}{\sqrt{2M_R \omega_{\mathbf{q}\nu}}} \left\langle \mathbf{k} + \mathbf{q}, j' \left| \frac{\delta V_{\text{eff}}}{\delta R_\nu} \right| \mathbf{k}, j \right\rangle, \quad (\text{A6})$$

which describes the electron-phonon matrix element for the scattering between the electronic states $|\mathbf{k}, j\rangle$ and $|\mathbf{k} + \mathbf{q}, j'\rangle$ through the phonon mode $|\mathbf{q}, \nu\rangle$, $\eta_{\mathbf{q}\nu}(R, \nu)$ is the normalized eigenvector of the phonon mode ($\mathbf{q}\nu$), M_R is the mass of the R th atom in the unit cell and $\delta V_{\text{eff}}/\delta R_\nu$ denotes the change in the total effective crystal potential with respect to the displacement of atom ν , and $|\mathbf{k}, j\rangle$ are the Kohn-Sham orbitals.

APPENDIX B: CONVERGE TEST OF PHONON

The phonon dispersion converges with $16 \times 16 \times 1$ \mathbf{k} mesh and $8 \times 8 \times 1$ \mathbf{q} mesh as shown in Fig. 6.

APPENDIX C: SPATIAL DECAY OF ELECTRONIC HAMILTONIAN, DYNAMICAL MATRIX, AND ELECTRON-PHONON MATRIX ELEMENTS

As presented in Fig. 7. The average spread of final Wannier functions is 1.05 \AA . The electronic Hamiltonian $\|H(R)\|$, dynamical matrix $\|D(R)\|$ and electron-phonon matrix elements $g(\text{Re}, 0)$ in the Wannier representation show exponential decay with increasing R . The ratios between $\|H(R = 15 \text{ \AA})\|$ and $H(0)$ decrease to 1.36×10^{-4} . The error in constructing the electron Hamiltonian introduced by Fourier interpolation is less than 0.02%.

APPENDIX D: CONVERGE TEST OF ELECTRON-PHONON COUPLING STRENGTH AND SUPERCONDUCTING GAP WITH \mathbf{k} AND \mathbf{q} GRIDS

It can be seen from Figs. 8(a) and 8(b) that the superconducting gap and anisotropical electron-phonon coupling strength

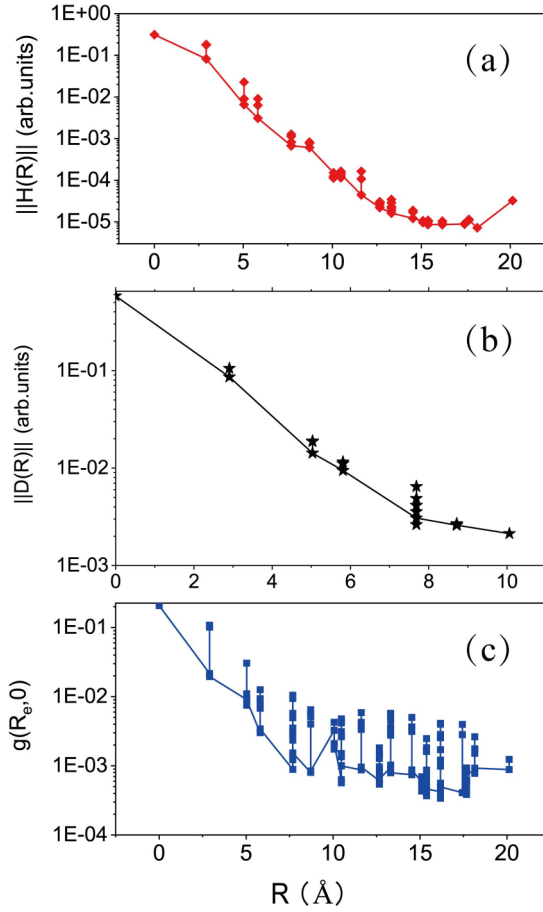


FIG. 7. Spatial decay of (a) electronic Hamiltonian $\|H(R)\|$, (b) dynamical matrix $\|D(R)\|$ and (c) electron-phonon matrix elements $g(\text{Re},0)$ and in the Wannier representation.

at $T = 10$ K converges with $156 \times 156 \times 1$ \mathbf{k} mesh and $78 \times 78 \times 1$ \mathbf{q} mesh.

APPENDIX E: MAIN SUPERCONDUCTING PARAMETERS

Table I displays the main superconducting parameters for monolayer W_2N_3 . T_c 's can not be derived for 0.1 hole/cell doped and 0.5% tensile strained cases due to obvious imaginary phonon.

TABLE I. Comparison of density of states (DOS) at Fermi level $N(E_F)$, logarithmic average of the phonon frequencies ω_{log} , electron-phonon coupling (EPC) constant λ , and superconducting transition temperature T_c of monolayer W_2N_3 based on the Allen-Dynes equation. All calculations are done with $\text{degauss} = 0.02$ Ry.

	$N(E_F)$ (states/spin/Ry/cell)	ω_{log} (K)	λ	$\mu^* = 0.10$			$\mu^* = 0.17$		
				f_1	f_2	T_c	f_1	f_2	T_c
Pristine	13.625	155.785	1.815	1.11	1.06	24.58	1.09	1.04	20.06
0.1 e/cell	13.106	187.411	1.435	1.08	1.03	22.76	1.07	1.02	17.55
0.1 h/cell	14.184	91.660	2.904	—	—	—	—	—	—
$\varepsilon = 0.5\%$	13.925	119.671	2.649	—	—	—	—	—	—
$\varepsilon = -0.5\%$	13.356	186.590	1.42	1.08	1.03	22.43	1.06	1.02	17.07
$\varepsilon = -2\%$	12.733	239.258	0.893	1.04	1.00	14.38	1.03	1.00	8.98
Hydrogen passivation	13.523	349.674	1.066	1.06	1.03	29.21	1.04	1.02	22.27

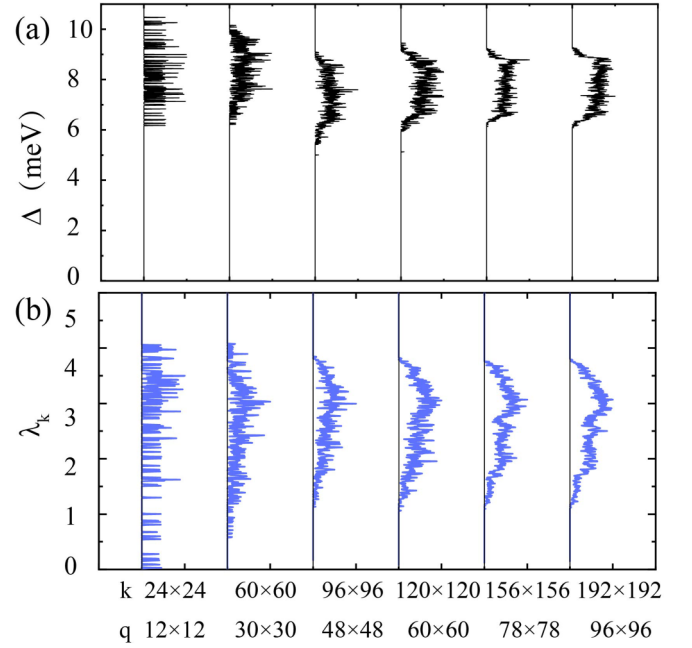


FIG. 8. Distribution of the (a) superconducting gap at $T = 10$ K and (b) anisotropic electron-phonon coupling strength with various uniform \mathbf{k} and \mathbf{q} meshes.

APPENDIX F: SPIN TEXTURE AT THE FERMI LEVEL IN MONOLAYER W_2N_3

As shown in Fig. 9. The spin polarization along $\langle S_x \rangle$ is nonzero only along the Γ - M direction, the component along $\langle S_y \rangle$ is completely zero.

APPENDIX G: DOPING AND STRAIN EFFECT

Charge doping shifts the Fermi energy and changes the $N(E_F)$. The small pockets crossing the Fermi level along $1/2M$ - M is changed. This part of bands is composed mainly of out-of-plane orbitals ($W d_{xz} + d_{yz} + d_{z^2}$ and outer layer $N p_z$) and part of the outer layer $N p_x + p_y$ states. By comparing the phonon dispersion of electron-doped with undoped systems in Figs. 10(b) and 10(e), one can infer that the most pronounced change is the hardening of the Raman active E'' phonon (in-plane vibration of the outer N atoms against each other leaves

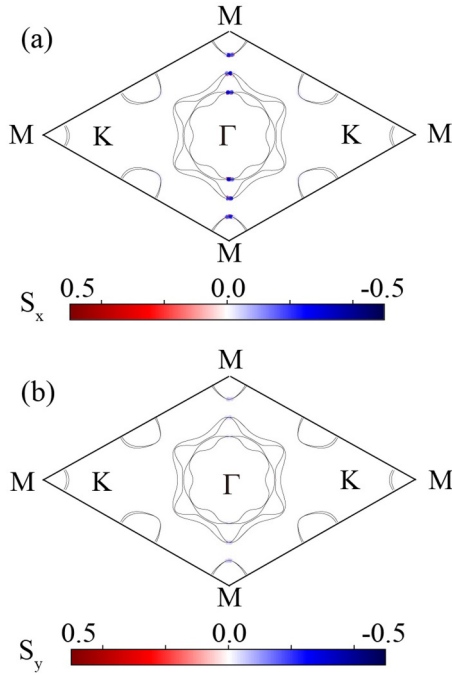


FIG. 9. Spin texture at the Fermi level in monolayer W_2N_3 . The color in (a) and (b) represents the in-plane spin polarization along $\langle S_x \rangle$ and $\langle S_y \rangle$.

the middle N atoms stationary) at 430 cm^{-1} near Γ and the ZA mode at $1/2K$. Therefore, the electron-phonon coupling (EPC) of the γ mode weakens. The contribution of EPC from phonons lower than 100 cm^{-1} decreases to 0.84 due to the narrowing and lowering of the $\alpha^2F(\omega)$ function peaks. Mean-

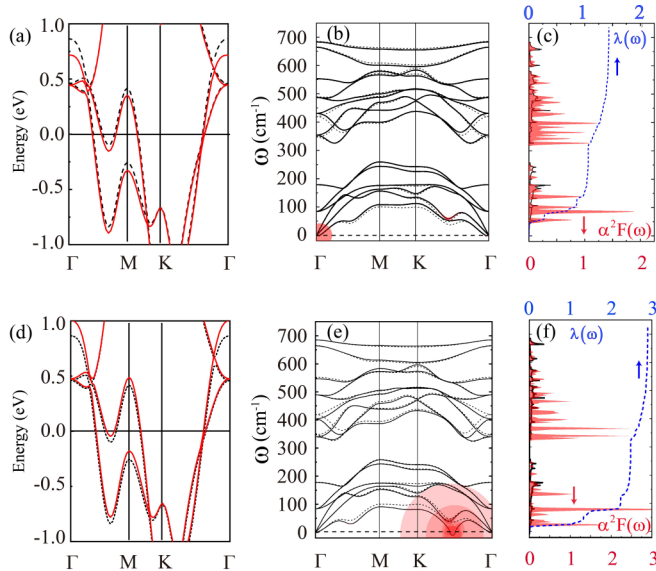


FIG. 10. (a) and (d) Electronic band structure. (b) and (e) Phonon dispersion decorated with red dots proportional to the partial electron-phonon coupling strength λ_{qv} . (c) and (f) Phonon density of states, isotropic Eliashberg spectral functions $\alpha^2F(\omega)$, and cumulative frequency-dependent coupling $\lambda(\omega)$. (a)–(c) 0.1 e/cell doped monolayer W_2N_3 , (d)–(f) 0.1 h/cell doped monolayer W_2N_3 . Dashed lines in (a), (d) and (b), (e) represent the band structure and phonon spectra of pristine monolayer W_2N_3 .

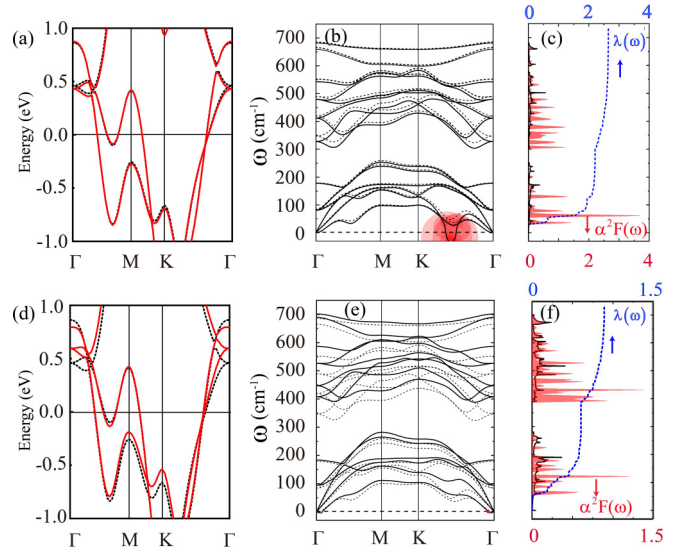


FIG. 11. (a) and (d) Electronic band structure. (b) and (e) Phonon dispersion decorated with red dots proportional to the partial electron-phonon coupling strength λ_{qv} . (c) and (f) Phonon density of states, isotropic Eliashberg spectral functions $\alpha^2F(\omega)$, and cumulative frequency-dependent coupling $\lambda(\omega)$. (a)–(c) 0.5% tensile strained. (d)–(f) 2.0% compressive strained monolayer W_2N_3 . Dashed lines in (a), (d) and (b), (e) represent the band structure and phonon spectra of pristine monolayer W_2N_3 .

while, the total EPC decreases by 21% from 1.815 to 1.435. Hole doping softens the E'' phonon near the Γ point and the ZA mode around $1/2K$. The latter phonon becomes imaginary accompanied with an extremely strong EPC [Fig. 10(e)].

Here, 0.5% tensile biaxial strain results in an overall softening of the phonons [Fig. 11(b)], which is beneficial to enhancing EPC (the EPC of the phonon at the β point is so large that it becomes negative). Also, 2% compressive strain shortens the bonds between inner (outer) N and W atoms by 1.03% (0.60%). It can be seen that both tensile and compressive strains affect the inner N atoms more substantially. On one hand, compressive strains widen the bands near the Fermi level [Fig. 11(d)], which decreases the $N(E_F)$. On the other hand, the shortening of all the N-W bonds give rise to an overall hardening of the phonons [Fig. 11(e)]. Those two factors lead to a 49% reduction of the EPC strength [Fig. 11(f)] and a hardening of ω_{\log} . As T_c is logarithmically related to λ , T_c finally reduced to 13.83 K.

APPENDIX H: STABILITY OF MONOLAYER $W_2N_3-H_2$

Thermodynamic (energetic) stability: The energy of the H_2 molecule is -6.765 eV , and the distance of two hydrogen atoms is 0.75 \AA , a good fit with the experimental value of 0.74 \AA . The total energy of the $W_2N_3-H_2$ monolayer ($-60.226\text{ eV/unit cell}$) is $1.914\text{ eV/unit cell}$ lower than the total energy of the W_2N_3 monolayer ($-51.547\text{ eV/unit cell}$) and the H_2 molecule (-6.765 eV). Therefore, the decomposing $W_2N_3-H_2$ monolayer into a W_2N_3 monolayer and H_2 gas is energetically unfavorable.

Thermal stability: The thermal stability of monolayer $W_2N_3-H_2$ was examined by *ab initio* molecular dynamics (AIMD) simulations in 300 K. As presented in Fig. 12, the

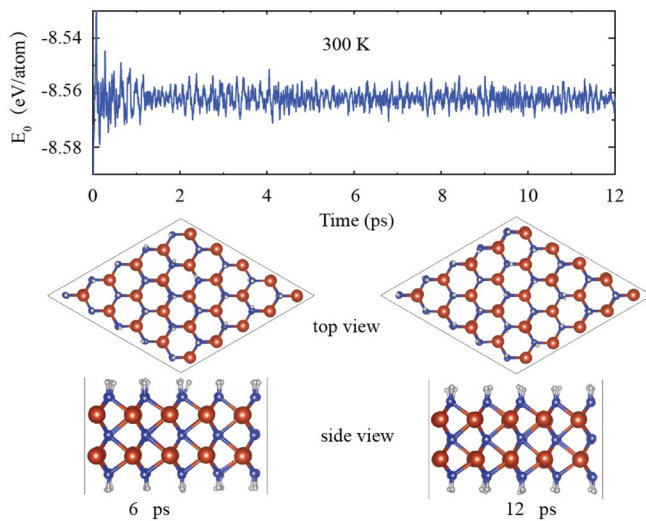


FIG. 12. Variation of total potential energy E_0 with time during *ab initio* molecular simulation of monolayer $W_2N_3-H_2$ at 300 K and the top and side view of the structure at 6 and 12 ps.

structures at 6 and 12 ps nearly remain the same atomic positions as the original structure with only tiny movement of the hydrogen atoms, suggesting thermal stabilities at ambient condition.

Dynamical stability: The phonon dispersion and phonon density of states shown in Figs. 5(c) and 5(d) demonstrate that all phonon frequencies are positive.

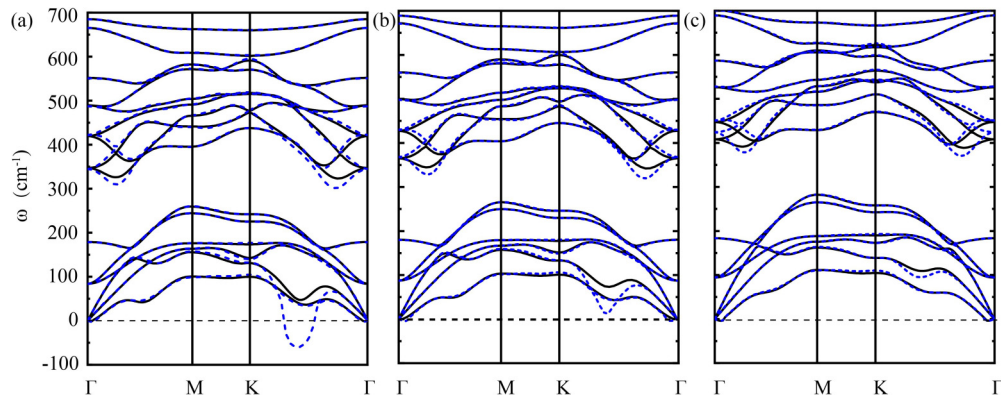


FIG. 13. Phonon dispersion of (a) pristine, (b) $\varepsilon = -0.5\%$, (c) $\varepsilon = -2\%$ strained monolayer W_2N_3 . Solid black lines and blue dashed lines are calculated with Methfessel-Paxton smearing of 0.02 and 0.008 Ry, respectively.

TABLE II. Calculated elastic constants C_{ij} and Young's modulus $E_{x(y)}$ (in $N m^{-1}$) of W_2N_3 and $W_2N_3-H_2$ monolayers.

	C_{11}	C_{22}	$C_{12} = C_{21}$	C_{66}	$E_{x(y)}$
$W_2N_3-H_2$	382.9	382.9	80.8	151.1	365.9
W_2N_3	403.8	403.8	159.6	122.1	340.7
	406.4 ^a	405.5 ^a	156.4 ^a	124.8 ^a	
Graphene	358.1	358.1	61.7	146.7	347.5
	358.1 ^b	358.1 ^b	60.4 ^b	148.9 ^b	348 ^b

^aReference [34].

^bReference [69].

Mechanical stability: As shown in Table II, all these elastic constants comply well with requirements of the mechanical stability criterion of a two-dimensional material [68]: $C_{11} * C_{22} - C_{12} * C_{21} > 0$ and $C_{66} > 0$, indicating that monolayer $W_2N_3-H_2$ is mechanically stable. Note that the elastic constant of graphene and monolayer W_2N_3 agrees well with previous papers [34,69], demonstrating the reliability of our calculations.

APPENDIX I: PHONON DISPERSION WITH DIFFERENT SMEARING

Biaxial compressive strain can efficiently suppress the CDW transformation tendency as can be seen from the evolution of phonon dispersion in Fig. 13.

- [1] M. Strongin, R. Thompson, O. Kammerer, and J. Crow, *Phys. Rev. B* **1**, 1078 (1970).
- [2] K. S. Novoselov, A. K. Geim, S. V. Morozov, D. Jiang, Y. Zhang, S. V. Dubonos, I. V. Grigorieva, and A. A. Firsov, *Science* **306**, 666 (2004).
- [3] C. Si, Z. Liu, W. Duan, and F. Liu, *Phys. Rev. Lett.* **111**, 196802 (2013).
- [4] S. Zeng, Y. Zhao, G. Li, and J. Ni, *Phys. Rev. B* **94**, 024501 (2016).
- [5] Y. Ge, W. Wan, F. Yang, and Y. Yao, *New J. Phys.* **17**, 035008 (2015).
- [6] G. Profeta, M. Calandra, and F. Mauri, *Nature Phys.* **8**, 131 (2012).
- [7] G. Huang, Z. Xing, and D. Xing, *Phys. Rev. B* **93**, 104511 (2016).
- [8] G. Huang, Z. Xing, and D. Xing, *Appl. Phys. Lett.* **106**, 113107 (2015).
- [9] J. Ye, Y. J. Zhang, R. Akashi, M. S. Bahramy, R. Arita, and Y. Iwasa, *Science* **338**, 1193 (2012).
- [10] J. M. Lu, O. Zheliuk, I. Leermakers, N. F. Q. Yuan, U. Zeitler, K. T. Law, and J. T. Ye, *Science* **350**, 1353 (2015).
- [11] K. Li, X. Feng, W. Zhang, Y. Ou, L. Chen, K. He, L.-L. Wang, L. Guo, G. Liu, and Q.-K. Xue, *Appl. Phys. Lett.* **103**, 062601 (2013).
- [12] M. Xue, G. Chen, H. Yang, Y. Zhu, D. Wang, J. He, and T. Cao, *J. Am. Chem. Soc.* **134**, 6536 (2012).

- [13] R. Zhang, J. Waters, A. K. Geim, and I. V. Grigorieva, *Nat. Commun.* **8**, 15036 (2017).
- [14] X. Xi, Z. Wang, W. Zhao, J.-H. Park, K. T. Law, H. Berger, L. Forró, J. Shan, and K. F. Mak, *Nat. Phys.* **12**, 139 (2016).
- [15] H. Wang, X. Huang, J. Lin, J. Cui, Y. Chen, C. Zhu, F. Liu, Q. Zeng, J. Zhou, P. Yu, X. Wang, H. He, S. H. Tsang, W. Gao, K. Suenaga, F. Ma, C. Yang, L. Lu, T. Yu, E. H. T. Teo, G. Liu, and Z. Liu, *Nat. Commun.* **8**, 394 (2017).
- [16] C. Sergio, M. R. Sinko, D. P. Gopalan, N. Sivadas, K. L. Seyler, K. Watanabe, T. Taniguchi, A. W. Tsen, X. Xu, and D. Xiao, *Nat. Commun.* **9**, 1427 (2018).
- [17] J. Cui, P. Li, J. Zhou, W.-Y. He, X. Huang, J. Yi, J. Fan, Z. Ji, X. Jing, F. Qu, Z. G. Cheng, C. Yang, L. Lu, K. Suenaga, J. Liu, K. T. Law, J. Lin, Z. Liu, and G. Liu, *Nat. Commun.* **10**, 2044 (2019).
- [18] C. Xu, L. Wang, Z. Liu, L. Chen, J. Guo, N. Kang, X.-L. Ma, H.-M. Cheng, and W. Ren, *Nat. Mater.* **14**, 1135 (2015).
- [19] E. S. Penev, A. Kutana, and B. I. Yakobson, *Nano Lett.* **16**, 2522 (2016).
- [20] M. Gao, Q.-Z. Li, X.-W. Yan, and J. Wang, *Phys. Rev. B* **95**, 024505 (2017).
- [21] S.-Y. Xie, Y. Wang, and X.-B. Li, *Adv. Mater.* **31**, 1900392 (2019).
- [22] M. Gao, X.-W. Yan, J. Wang, Z.-Y. Lu, and T. Xiang, *Phys. Rev. B* **100**, 024503 (2019).
- [23] J. Bekaert, A. Aperis, B. Partoens, P. M. Oppeneer, and M. V. Milošević, *Phys. Rev. B* **96**, 094510 (2017).
- [24] J. Bekaert, M. Petrov, A. Aperis, P. M. Oppeneer, and M. V. Milošević, *Phys. Rev. Lett.* **123**, 077001 (2019).
- [25] J. Nagamatsu, N. Nakagawa, T. Muranaka, Y. Zenitani, and J. Akimitsu, *Nature* **410**, 63 (2001).
- [26] H. Yu, X. Yang, X. Xiao, M. Chen, Q. Zhang, L. Huang, J. Wu, T. Li, S. Chen, L. Song, L. Gu, B. Y. Xia, G. Feng, J. Li, and J. Zhou, *Adv. Mater.* **30**, 1805655 (2018).
- [27] G. Paolo *et al.*, *J. Phys.: Condens. Matter* **21**, 395502 (2009).
- [28] J. P. Perdew, K. Burke, and M. Ernzerhof, *Phys. Rev. Lett.* **77**, 3865 (1996).
- [29] S. Baroni, S. de Gironcoli, A. Dal Corso, and P. Giannozzi, *Rev. Mod. Phys.* **73**, 515 (2001).
- [30] M. Methfessel and A. T. Paxton, *Phys. Rev. B* **40**, 3616 (1989).
- [31] N. Marzari, D. Vanderbilt, A. De Vita, and M. C. Payne, *Phys. Rev. Lett.* **82**, 3296 (1999).
- [32] H. Jin, L. Li, X. Liu, C. Tang, W. Xu, S. Chen, L. Song, Y. Zheng, and S.-Z. Qiao, *Adv. Mater.* **31**, 1902709 (2019).
- [33] N. Mounet, M. Gibertini, P. Schwaller, D. Campi, A. Merkys, A. Marrazzo, T. Sohler, I. E. Castelli, A. Cepellotti, and G. Pizzi, *Nat. Nanotechnol.* **13**, 246 (2018).
- [34] W. Jin, W. Sun, X. Kuang, C. Lu, and L. Kou, *J. Phys. Chem. Lett.* **11**, 9643 (2020).
- [35] S. Wang, X. Yu, Z. Lin, R. Zhang, D. He, J. Qin, J. Zhu, J. Han, L. Wang, and H.-k. Mao, *Chem. Mater.* **24**, 3023 (2012).
- [36] G. Eliashberg, *Sov. Phys. J. Exp. Theor. Phys.* **11**, 696 (1960).
- [37] P. B. Allen, *Phys. Rev. B* **6**, 2577 (1972).
- [38] P. B. Allen and R. C. Dynes, *Phys. Rev. B* **12**, 905 (1975).
- [39] C. F. Richardson and N. W. Ashcroft, *Phys. Rev. Lett.* **78**, 118 (1997).
- [40] D. Y. Kim, R. H. Scheicher, C. J. Pickard, R. J. Needs, and R. Ahuja, *Phys. Rev. Lett.* **107**, 117002 (2011).
- [41] S. Sarkar, N. Kulkarni, R. Kulkarni, K. Thekkepat, U. Waghmare, and P. Ayyub, *Nano Lett.* **17**, 7027 (2017).
- [42] E. V. Castro, H. Ochoa, M. I. Katsnelson, R. V. Gorbachev, D. C. Elias, K. S. Novoselov, A. K. Geim, and F. Guinea, *Phys. Rev. Lett.* **105**, 266601 (2010).
- [43] M. V. Fischetti and W. G. Vandenberghe, *Phys. Rev. B* **93**, 155413 (2016).
- [44] E. R. Margine and F. Giustino, *Phys. Rev. B* **90**, 014518 (2014).
- [45] X.-T. Jin, X.-W. Yan, and M. Gao, *Phys. Rev. B* **101**, 134518 (2020).
- [46] A. Y. Liu, I. I. Mazin, and J. Kortus, *Phys. Rev. Lett.* **87**, 087005 (2001).
- [47] W. Kohn, *Phys. Rev. Lett.* **2**, 393 (1959).
- [48] I. Bersuker, *The Jahn-Teller Effect* (Cambridge University Press, Cambridge, 2006).
- [49] C. Heil, S. Poncé, H. Lambert, M. Schlipf, E. R. Margine, and F. Giustino, *Phys. Rev. Lett.* **119**, 087003 (2017).
- [50] Z. P. Yin, A. Kutepov, and G. Kotliar, *Phys. Rev. X* **3**, 021011 (2013).
- [51] M. Lazzeri, C. Attacalite, L. Wirtz, and F. Mauri, *Phys. Rev. B* **78**, 081406 (2008).
- [52] M. Calandra, P. Zocante, and F. Mauri, *Phys. Rev. Lett.* **114**, 077001 (2015).
- [53] T. Das and K. Dolui, *Phys. Rev. B* **91**, 094510 (2015).
- [54] J. Bekaert, A. Aperis, B. Partoens, P. M. Oppeneer, and M. V. Milosevic, *Phys. Rev. B* **97**, 014503 (2018).
- [55] Z. Li, G. Antonius, M. Wu, F. H. da Jornada, and S. G. Louie, *Phys. Rev. Lett.* **122**, 186402 (2019).
- [56] B. S. Chandrasekhar, *Appl. Phys. Lett.* **1**, 7 (1962).
- [57] A. M. Clogston, *Phys. Rev. Lett.* **9**, 266 (1962).
- [58] F. Giustino, M. L. Cohen, and S. G. Louie, *Phys. Rev. B* **76**, 165108 (2007).
- [59] S. Poncé, E. R. Margine, C. Verdi, and F. Giustino, *Comput. Phys. Commun.* **209**, 116 (2016).
- [60] Y. Zhao, S. Zeng, C. Lian, Z. Dai, S. Meng, and J. Ni, *Phys. Rev. B* **98**, 134514 (2018).
- [61] H. J. Choi, D. Roundy, H. Sun, M. L. Cohen, and S. G. Louie, *Phys. Rev. B* **66**, 020513 (2002).
- [62] Y. Zhao, C. Lian, S. Zeng, Z. Dai, S. Meng, and J. Ni, *Phys. Rev. B* **100**, 094516 (2019).
- [63] H. J. Choi, D. Roundy, H. Sun, M. L. Cohen, and S. G. Louie, *Nature* **418**, 758 (2002).
- [64] E. R. Margine and F. Giustino, *Phys. Rev. B* **87**, 024505 (2013).
- [65] D. Mou, R. Jiang, V. Taufour, S. L. Bud'ko, P. C. Canfield, and A. Kaminski, *Phys. Rev. B* **91**, 214519 (2015).
- [66] R. Bianco, I. Errea, L. Monacelli, M. Calandra, and F. Mauri, *Nano Lett.* **19**, 3098 (2019).
- [67] N. Marzari, A. A. Mostofi, J. R. Yates, I. Souza, and D. Vanderbilt, *Rev. Mod. Phys.* **84**, 1419 (2012).
- [68] F. Mouhat and F.-X. Coudert, *Phys. Rev. B* **90**, 224104 (2014).
- [69] X. Wei, B. Fragneaud, C. A. Marianetti, and J. W. Kysar, *Phys. Rev. B* **80**, 205407 (2009).